Design, Performance Evaluation, and Modeling of an Ultrahigh Resolution Detector Dedicated for Simultaneous SPECT/MRI

Xiaochun Lai, Liang Cai, Jia-Wei Tan, Elena Maria Zannoni, Boris Odintsov, and Ling-Jian Meng, *Member, IEEE*

***Abstract*—In this article, we report design and preliminary performance evaluation of a CdTe detector module for use in an MR-compatible preclinical single-photon emission computed tomography system. The detector module consists of four CdTe detectors. Each of them has a CdTe crystal with a dimension of 1.125 cm × 2.25 cm × 2 mm (thickness). The crystal anode side is divided into 32 × 64 square pixels with a width of 350 μm and attached to a custom-designed energy-resolved photon-counting (ERPC) application-specific integrated circuitry. The ERPC CdTe detector module has a median energy resolution of 7.0 keV across 8192 (4 × 32 × 64) pixels and 95% of the pixels have energy resolution better than 9 keV inside a Siemens clinical 3-T MR scanner; it has a median detection efficiency of 0.47 and 95% of the pixels have detection efficiency between 0.44 and 0.49; the detector spatial resolution enables one to observe the point response function (PRF) distortion caused by a 3T magnetic field. An analytical method has been developed to model this distortion and the corresponding modeled PRF has a root of mean-square error within 5%, compared to the experimental PRF.**

***Index Terms*—ASIC, CdTe, CZT, photon counting, SPECT, SPECT/MRI.**

I. Introduction

THE COMBINATION of single-photon emission computed tomography (SPECT) or positron emission tomography (PET) with magnetic resonance imaging (MRI) shows powerful capability in both preclinical research and clinical applications, since it harnesses the complementary nature of different modalities on an integrated imaging platform. Many studies have elaborated the value and clinical use of combined PET/MRI [1]–[13], but to date the development of SPECT and MRI has stayed in preclinical stage, and only one simultaneous clinical prototype has been reported [14]. There are several technical obstacles faced by researchers to truly integrate SPECT instrumentation with MR scanners without degrading the original optimum performance of either.

First, SPECT performance would severely degrade because SPECT detector functioning could be affected by the strong magnetic field, rapidly switching gradient fields, and the RF field of an MR scanner. On the other hand, these MR fields are prone to distortion due to the electronic, metallic or ferromagnetic components of the detectors and collimators, which results in degraded MR images [6], [15]–[17]. Another main challenge of merging these two modalities is space constraints [18]. Due to the very limited space inside MR scanners, a compact SPECT system with low magnification design is required because the conventional pinhole SPECT system with large magnification is too bulky. To maintain high SPECT spatial resolution in this compact design, an ultrahigh resolution detector (sub-mm or even sub-500 μm) is required. Finally, any moving part inside a strong magnetic field is likely to create artifacts in MR images. Thus, a stationary SPECT scanner is preferred to the conventional rotating design. It imposes additional constraints to the volume of the detector design [18].

In addition to developing an MRI compatible collimators [17], [19]–[21], another key to overcome these challenges is to develop detectors with high resolution, compact geometry, and MRI compatibility. One approach is based on a scintillator detector coupled with SiPM [22]–[25]. The ultrahigh resolution is achieved by cutting the crystal into a sub-mm pixel. The INSERT project, which several groups in EU are working on, aims to develop preclinical and clinical SPECT/MRI systems for chemotherapy, and is on this path [14], [21], [25]–[29]. The project developed a sub-mm resolution detector using CsI (TI) with SiPM readout [25]. The detector achieves an energy resolution of 12%–14% full width at half maximum (FWHM) at 140 keV and a high spatial resolution of 1-mm FWHM [25]. The study also shows that this detector has minimum impact over MR image quality and achieves a good MRI compatibility [21]. The preclinical scanner based on this detector has achieved a resolution of 0.9 mm across 15.6-mm FOV and a

Manuscript received January 20, 2020; revised May 22, 2020, September 21, 2020, and December 9, 2020; accepted January 19, 2021. Date of publication January 22, 2021; date of current version December 30, 2021. This work was supported by NIBIB under Grant R01EB011640. *(Corresponding author: Xiaochun Lai.)*

Xiaochun Lai, Liang Cai, and Jia-Wei Tan are with the Department of Nuclear, Plasma and Radiological Engineering, University of Illinois at Urbana–Champaign, Champaign, IL 61801 USA (e-mail: xlai2@illinois.edu).

Elena Maria Zannoni is with the Department of Bioengineering, University of Illinois at Urbana–Champaign, Champaign, IL 61801 USA.

Boris Odintsov is with the Beckman Institute for Advanced Science and Technology, University of Illinois at Urbana–Champaign, Champaign, IL 61801 USA

Ling-Jian Meng is with the Department of Nuclear, Plasma and Radiological Engineering, University of Illinois at Urbana–Champaign, Champaign, IL 61801 USA, also with the Department of Bioengineering, University of Illinois at Urbana–Champaign, Champaign, IL 61801 USA, and also with the Beckman Institute for Advanced Science and Technology, University of Illinois at Urbana–Champaign, Champaign, IL 61801 USA.

Color versions of one or more figures in this article are available at https://doi.org/10.1109/TRPMS.2021.3053592.

Digital Object Identifier 10.1109/TRPMS.2021.3053592

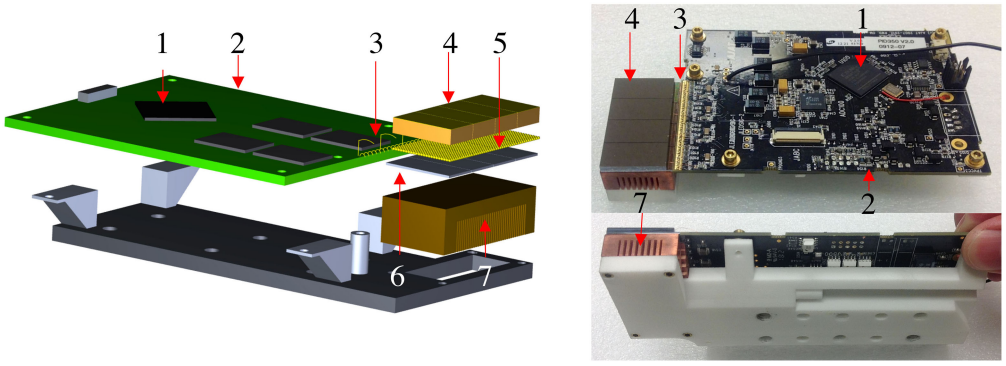

Fig. 1. ERPC detector module for SPECT/MRI applications. (Left) 3-D drawing and (right) actual module. (1) ACTEL FPGA; (2) PCB; (3) wire bounding connecting PCB and ASICs; (4) four CdTe crystals, each with volume of 1.125 cm × 2.25 cm × 2 mm; (5) SnBI solder connecting the CdTe anode to corresponding pixel circuitry in the ASIC; (6) four ASICs, each with 32 × 64 channels; and (7) cooper heat sink.

sensitivity of 0.11% with a multiple-pinhole collimator (nine holes of 0.8 mm × 0.8 mm) [28]. The clinical scanner achieves a spatial resolution of 8 mm and a sensitivity of 0.036% using multiple slit-slat collimator [29].

An alternative approach is using semiconductor (CdTe/CZT) detectors. Comparing to the scintillator detector, the CdTe/CZT detector can achieve better spatial resolution and energy resolution [30]. However, the detector response could be distorted in strong static magnetic field inside an MR scanner [31], [32]. Wagenaar *et al.* reported a CZT detector for SPECT/MRI applications. The detector has a spatial resolution of about 1.5 mm and an energy resolution of 5% at 122 keV [33]. The feasibility of using this detector for SPECT/MRI application has first been demonstrated by Hamamura *et al.* [31]. The same detector is used by Tsui *et al.*'s group to develop the whole-body small-animal SPECT/MRI insert, which has a spatial resolution of 3 to 5 mm [34]. Later Tsui *et al.*'s group further optimized the system design and build a another SPECT/MRI insert using the same detector [35]. The system achieves a resolution of around 1.1 mm using 32 pinholes with a diameter of 0.5 mm [35].

We have developed an energy-resolved photon-counting (ERPC) CdTe detector. This ERPC detector offers an intrinsic spatial resolution of 350 μm and an energy resolution of 3–4 keV at 122 keV [36]. Based on this work, we developed an ERPC detector dedicated for SPECT/MRI applications. In this article, we reported the design and the intrinsic performance of this detector module. We also evaluated the impact of the MRI fields (high static magnetic field, rapidly switching gradient fields and RF field) over the detector performance in terms of spatial, energy response, detection efficiency, and uniformity. We also developed an analytical modeling method to minimize the impact of the distortion induced by MRI.

II. Method and Materials

A. Basic Detector and Electronics Design

Fig. 1 shows the detector module that we have developed specifically for use in SPECT/MRI applications and Fig. 2(b) shows the detector system outline. The detector module offers a total detection area of 2.25 cm × 4.5 cm. It consists of 4 CdTe sensors provided by Acrorad [37], each with a size of 1.125 cm × 2.25 cm × 2 mm. The anode side of the CdTe detector is divided into 32 × 64 pixels of 350-μm pitch. The CdTe detector uses gold (ohmic) contacts, and the dimension of each pixel is 300 μm × 300 μm in size, leaving a gap of 50 μm in width between adjacent pixels. The CdTe crystal is biased at −350 V.

TABLE I
Specifications of ERPC ASIC for SPECT/MRI Applications

Physical Dimensions	1.125 × 2.25 cm^2, 32 × 64 pixels
Pixel Size	350 × 350 μm^2
Preamp Gain	10 μV/electron
Shaping Time	∼1 μs
ADC	8 bit
Frame Rate	50 frame per second
Max Readout Count Rate	50 cps per pixel
Energy Resolution with 2 mm CdTe	7 keV@122 keV (Measured)
Dynamic Range	35∼250 keV

The anode pixels are stud bonded to a custom-designed application-specific integrated circuitry (ASIC). Details about this ASIC's specification can be found in Table I. This ASIC is fabricated using 0.35-μm technology and has 32 × 64 channels, which matches the 32 × 64 anode pixel pattern with 350-μm pitch. For each channel of the ASIC, the pixel circuitry [Fig. 2(a)] have a bonding pad with a diameter of 25 μm and a preamplifier with a feedback capacitor of 16 fF. The corresponding gain is 10 μV per electron. For a 140-keV photon (Tc-99m), there will be 3.2×10^4 electrons and the corresponding voltage of the signal is 0.33 V.

The output of preamplifier is filtered by a shaping amplifier with a time constant of 1 μs. The time constant is determined by considering two factors. One factor is the signal pulse width. The shaping time should be much larger than pulse width to avoid ballistic deficit [38]. When the 2 mm CdTe with a 350-μm anode size is biased at −350 V, the signal pulse width would be in the range of 0.02–0.2 μs, depending on where it happens. The other factor is the detector counting capability. The shaping time should be small enough to meet the detector counting capability. The previous version ASIC [36] has maximum counting rate of 0.8 Mcps/pixel. So in the previous version of ASIC we used 1-μs time constant.

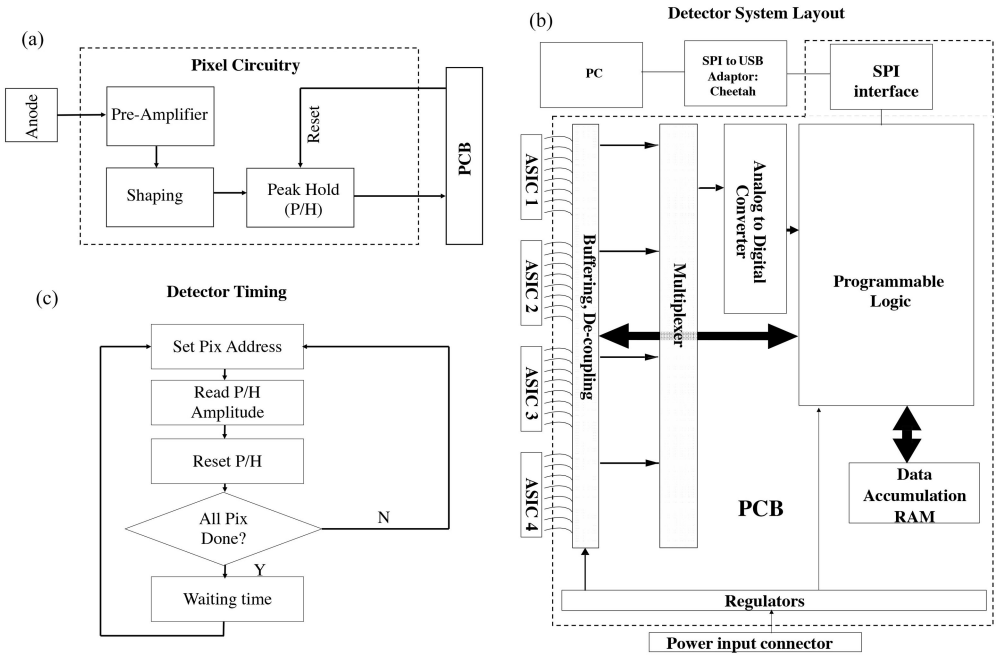

Fig. 2. MRI compatible ERPC detector system layout. (a) Pixel circuitry. (b) System architecture. (c) Pixel readout sequence.

To reduce design risk, we kept the same time constant in the current version.

The peak of the signal from the shaping amplifier will be held by the peak-hold unit in the pixel circuitry until it is readout by the ADC on the digital readout printed circuitry board (PCB) [Fig. 2(a) and (b), wire-bonded to the CdTe/ASIC hybrids]. The peak-hold unit will be reset after the signal readout and ready for the next events.

Unlike the previous ASIC [36], this one uses a clocked readout, rather than pixel-by-pixel ADC readout. It reduces design complexity and power consumption. The ERPC ASIC sends out the signal peak from the individual pixels one by one [Fig. 2(c)]. The trains of signals are digitized by an 8-bit ADC with 25-MHz sampling rate on the readout PCB [Figs. 1 and 2(b)]. The digitized signals are temporarily stored in a 32-MB flash memory [RAM in Fig. 2(b)] before sending to a remote PC through USB2 interface. A field programmable gate array (FPGA) located on the PCB synchronizes the readout operations. This readout scheme reduces pixel maximum readout rate from 0.8 Mcps per pixel [36] to 50 cps per pixel. In general, this readout rate is sufficient for an ultrahigh resolution preclinical SPECT system. Such system typically uses large magnification design. The event rates would be lower than 1 cps per pixel, which is much lower than that of clinical applications [39].

For SPECT/MRI applications, we minimized the usage of magnetic component and changed the layout of the board of the previous version [36]. We moved the wire-bonding pads to the edge of the PCB. This design choice would allow the detector to be assembled into a closely packed detector ring for use in a stationary SPECT system geometry. To make the detector compatible with MR scanners, we used ultrapure copper for the heat sink and 3-D printed polyethylene support structure. The support structure has hollow channels allowing compressed air to go through for cooling purpose (Fig. 1).

By design, the detector module can act as an independent unit that directly communicates with a data acquisition PC [Fig. 2(b)]. The PC is customized with 10–20 USB2 ports to interface with multiple detector modules and to potentially allow for a scalable detection system with 10–20 detector modules that could be readily tailored for preclinical SPECT/MRI applications.

B. Evaluating CdTe Detectors Outside and Inside 3 Tesla Clinical MR Scanner

1) Energy Resolution: Energy resolution was first measured outside an MRI scanner. 50 μCi Co-57 was used to irradiate the calibrated detector from a distance of around 7.8 cm. From the energy spectrum obtained on each pixel, the data points around 122-keV peak were fitted to an asymmetric Gaussian distribution. FWHM of the distribution was defined as energy resolution.

Energy resolution was also measured inside a Siemens Trio-I 3T scanner using exactly the same source and experimental settings as described above. To investigate the impact of the strong magnetic static field, the first detector data were collected when the MR scanner was not actively acquiring images. Another experiment was carried with MR scanner actively acquiring data using a gradient echo sequence (GRE) [40]. This allows us to evaluate the detector response under rapidly switching gradient field and RF field.

2) Detection Efficiency: To evaluate the detection efficiency, the 50 μCi Co-57 was used to irradiate the calibrated detector. The geometry relation between source and detector are precalibrated, i.e., the geometry information was known. The detector efficiency for pixel m (β_m) was calculated by

$$\beta_m = N_m / \overline{N}_m \tag{1}$$

$$\overline{N}_m = N \int_{S_m} \mathrm{d}\Omega \tag{2}$$

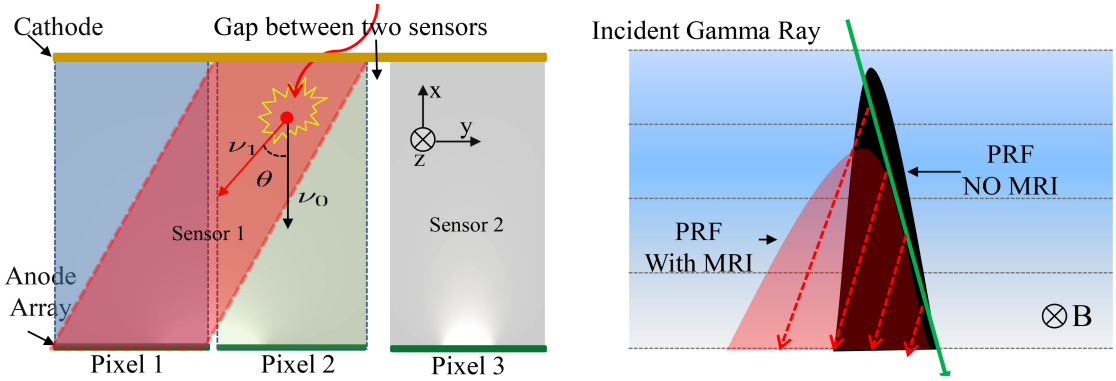

Fig. 3. Illustration of magnetic field distorting the electron transportation and PRF. Left is the transverse view of detector pixels. Pixel 1 and pixel 2 belong to Sensor 1, pixel 3 belongs to Sensor 2, and the gap exists between pixel 2 and pixel 3. The coordinate system is also defined in this figure, where x-axis is along the electric field and pointing toward the detector cathode, z-axis is along the scanner axis and with the same direction as B_0 field. The magnetic field $B = [0, 0, B_z]$ is along the z-axis, and the electric field $E = [E_x, 0, 0]$ is along x-axis. With presence of the magnetic field, the electrons generated by the gamma-ray interaction will drift along direction, which has fixed angle θ related to the electric field, which is described in (6). Right illustrates the charge transportation impact over the PRF. The red and black shaded parts represent two PRF profiles inside and outside MRI, respectively, when gamma rays interact with the sensor in specific incident angle.

where $\overline{N}_m$ is the expected incident counts of detector pixel m. It equals to product of emitted counts, N, and solid angle corresponding to pixel m. N_m is measured counts above 90 keV. Please note that a preclinical SPECT typically uses a wider energy window compared to clinical one, because scattering is not a severe issue in preclinical applications. To study MRI impact over the detection efficiency, the same experiment data sets as the energy performance were used. We compared the detection efficiency inside and outside MRI.

3) Point Response Function Measurement: To evaluate the spatial performance of the CdTe detector, we measured the point source projections point response function (PRF) through four 300 μm pinholes using the 50 μCi Co-57 point source. The geometry relation between the source, the pinholes and the detector was precalibrated, i.e., the geometry information was known. The detector was 7.8 cm away from the source. The four pinholes were placed 3.6 cm away from the source and distributed on a ring. Incident angles between gamma rays and the detector through each pinhole were $-2.2°$, $8.5°$, $16.4°$, and $25.5°$, respectively. The detector was carefully aligned so that z-axis in the detector coordinate system (defined in Fig. 3) was along the direction of the main magnetic field. We collected 15 min of data both outside and inside the MR scanner. During the inside MRI experiment, the scanner was actively taking image using a GRE sequence.

C. Modeling Detector Response Function Inside and Outside Strong Magnetic Field

For the MRC-SPECT-I system to achieve an ultrahigh imaging resolution, it is important to derive an accurate PRF for CdTe detectors when operated inside a strong magnetic field. In this section, we will discuss the steps that we used to derive the detector response function.

For a point source at distance $\boldsymbol{r_s}$, the total photons (H_m) detected by detector pixel m can be calculated by a widely used analytical model [41]–[43] given by

$$H_m = N \int_{r_d \in V_m} \left\{ \frac{\mu_d}{4\pi |\boldsymbol{r}_d - \boldsymbol{r}_s|^2} \times \exp\left[-\mu_d l_d(\boldsymbol{r}_d, \boldsymbol{r}_s) - \mu_d l_p(\boldsymbol{r}_d, \boldsymbol{r}_s)\right] \right\} dV \tag{3}$$

where H_m equals to the product of emitted counts, N, and detection probability of pixel m. The detector probability is integrated over the sensing volume belonging to detector pixel m, i.e., $\boldsymbol{r}_d \in V_m$. μ_d and μ_p are linear attenuation coefficients of CdTe and pinhole (made of 90% platinum and 10% iridium) at 122 keV, respectively. l_d and l_p are the gamma ray penetration length in CZT/CdTe and a pinhole, respectively.

Without presence of a magnetic field, charge carriers are assumed to drift along the electric field and the electric field can be assumed to be perpendicular to a detector pixel anode. Each pixel only collects events right above the pixel anode. For example, as illustrated in Fig. 3, pixel 1 only collects events from the corresponding sensing volume ([$\boldsymbol{r}_d \in V_m$ in (3)]) marked in blue in Fig. 3.

In presence of a magnetic field, the charge carrier transportation is distorted by both electric field ($E = [E_x, E_y, E_z]^T$) and magnetic field ($B = [B_x, B_y, B_z]^T$). The charge carrier drift velocity ($V = [v_x, v_y, v_z]^T$) is given by [44]

$$V = \frac{-\mu}{1 + \mu_H^2 B^2} ME \tag{4}$$

where M^1 is a matrix capturing magnetic field impact, where μ_H is the Hall mobility. For CdTe, it is approximately equal to charge carrier mobility μ. The CdTe detectors were well aligned inside the MR scanner so that the detector plane was parallel to the direction of the main magnetic field, B_0. Assuming x-direction is perpendicular to the detector surface and pointing toward the axis of the MR scanner, and

$$^1\begin{bmatrix} 1+\mu_H^2 B_x^2 & \mu_H^2 B_x B_y - \mu_H B_z & \mu_H^2 B_x B_z + \mu_H \cdot B_y \\ \mu_H^2 B_x B_y + \mu_H B_z & 1+\mu_H^2 \cdot B_y^2 & \mu_H^2 B_y B_z - \mu_H B_x \\ \mu_H^2 B_x B_z - \mu_H \cdot B_y & \mu_H^2 B_y B_z + \mu_H B_x & 1+\mu_H^2 B_z^2 \end{bmatrix}$$

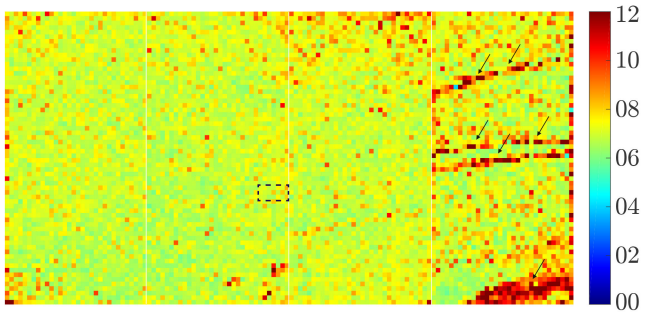

Fig. 4. Detector energy resolution at 122 keV. Co-57 point source (50 μCi) was placed 7.8 cm away and illuminated the detector for 20 min. The arrows point to the defect region. The spectra of the pixels (marked by the dash rectangle) are shown in Fig. 5. The right edges of the four sensors are marked by the white lines.

z-direction is parallel to the axis of the MR scanner (illustrated in Fig. 3), then $E = E_x$ and $B = B_z$. Therefore, (4) is simplified to

$$\begin{bmatrix} v_x \\ v_y \\ v_z \end{bmatrix} = K \cdot \begin{bmatrix} E_x \\ -\mu_H B_z E_x \\ 0 \end{bmatrix}. \tag{5}$$

Based on (5), the charge carriers always move in a direction with fixed angle θ as shown in Fig. 3 from the electric field $E = E_x$. θ can be calculated as

$$\theta = \arctan\left(\frac{v_y}{v_x}\right) = \arctan(-\mu_H B_z). \tag{6}$$

θ is equal to 18.2° for a 3T magnetic field. Therefore, the events collected by a pixel anode are no longer right above the corresponding sensing volume. It will distort PRF as shown in Fig. 3. To model the PRF inside an MRI scanner, the integration volume, $\boldsymbol{r}_d \in V_m$ in (4), has to be modified accordingly. As illustrated in Fig. 3, for pixel 1, instead of the blue marked region, the integration volume is the red marked region, which is titled by θ.

III. Results

Fig. 4 shows the energy performance of the detector module. For the detector module being evaluated in this study, we found less than five dead or hot pixels across 8192 pixels. The energy resolution in terms of FHWM at 122-keV peak has a median value of 7.0 keV and 95% of the pixels have an energy resolution better than 9 keV. 0.6% of them can degrade to worse than 12 keV. This degradation is mostly caused by the charge loss in defect regions (the regions pointed by black arrows in Fig. 4) or in the sensor edges [45]–[47]. The charge loss could be reduced by using a better quality CdTe sensor and improving edge fabrication and polishing technology.

Fig. 5 shows a comparison of the energy spectra between inside (blue and red) and outside (green) a Siemens Trio 3T MR scanner. While the presence of a strong magnetic field would with no doubt affect the charge collection process, it had a minor impact on the spectral response, except for those pixels at the right edge of each sensor (i.e., columns 32, 64, 96, and 128). As shown in Fig. 5, 3 × 6 spectra among 8192 spectra were selected. The detector spectra of outside and inside MRI were visually quite similar and the difference of counts above 90 keV was around 5% for pixels not at the right edge of each sensor. However, the spectra of the right edge pixels in each sensor were distorted by the magnetic fields and the detected counts were reduced by 69%. As illustrated in Fig. 3, it was because the charges generated by events at the right edge of Sensor 1 drifted toward the left, but the charge loss due to this drift can not be compensated as charges in Sensor 2 were not able to move to Sensor 1 because of the physical gap between two sensors.

Though the gradient field is much smaller than the main field, it rapidly changes, which could induce eddy current on the metal components of detector electronics, thus affects the detector functionality. But we did not observe a significant effect from the gradient field nor RF pulses by comparing spectra inside MRI with (red curves in Fig. 5) and without (blue curves in Fig. 5) an active GRE imaging sequence.

Fig. 6(a) shows the detection efficiency and uniformity across 8192 pixels. The detection efficiency has a median value of 0.47 and 95% of the pixels' detection efficiency is between 0.44 and 0.49. The detection efficiency is far less than 1, because of limited stopping power of 2 mm CdTe and charge sharing effect of small pixel design [48]–[53].

Fig. 6(b) shows the relative detection efficiency difference between inside the MR scanner with the gradient sequence and outside the MRI scanner. The strong magnetic field has minor impact in most of the pixels (with mean difference around 5.1%), except for those at the right edge of each sensor (i.e., columns 32, 64, 96, and 128). The detection efficiency of these pixels was reduced by 69% because of the same reason we discussed in the results of Fig. 5. Comparing results inside MRI with [Fig. 6(b)] and without [Fig. 6(c)] an active GRE imaging sequence, we did not observe a significant effect from the rapidly switching gradient fields and RF pulses.

Fig. 7 shows the projections of the point source through four pinholes with different incident angles. The high spatial resolution of the detector allows us to fully sample the PRF and to observe the MRI distortion effect. As shown in Fig. 7, the weighting center of PRF shifts around 0.92 pixel (322 μm) because of charge carrier drifting caused by the magnetic field.

Fig. 8 shows modeled PRF and experimental PRF. The modeled PRF matches well with the experimental one, for both inside MRI and outside MRI cases. The difference between the modeled and experimental PRFs was measured by root of mean-square error, which was derived from comparing the normalized counts obtained from the experiment (c_i) and from the model (c_i') within an energy window around the 122 keV peak as follows:

$$\chi = \frac{1}{I}\sqrt{\sum_{i}^{I}\left(c_i - c_i'\right)^2} \tag{7}$$

where I is the number of total pixel detected counts $> 1\%$ of the PRF peak. χ for outside and inside MRI are both around 5%.

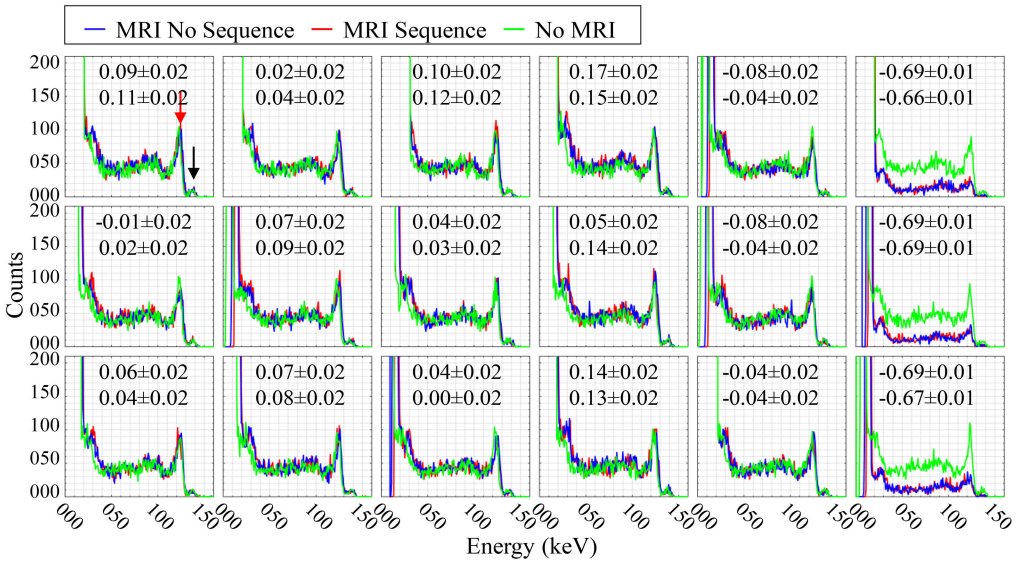

Fig. 5. Spectra of the pixels marked by the dash rectangle in Fig. 4. The data were acquired using Co-57 source around 50 μCi in 20 min. The green lines is taken outside the MR scanner, the red lines inside the MR scanner with gradient sequence, and the blue lines inside MRI without the active sequence. The red and black arrows in the left upper corner subplot show the 122 keV and 136 keV peaks, respectively. The numbers in each subfigure shows the relative counts change above 90 keV (energy bin positions are derived using the calibration outside MRI) compared with outside MRI results.

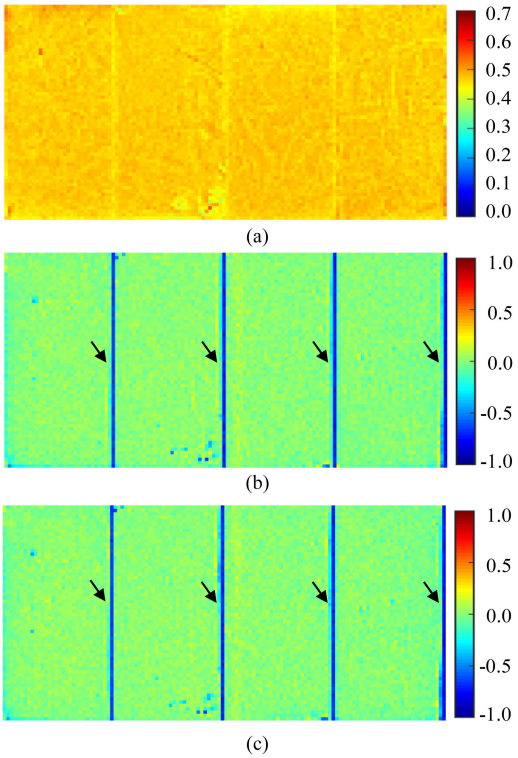

Fig. 6. (a) Detection efficiency outside MRI scanner, which is calculated by (1). (b) Relative detection efficiency difference between inside the MR scanner without any sequence and outside the MRI scanner. (c) Similar comparison, but the data taken inside the MR scanner has the gradient sequence. The arrows in (b) and (c) point to the pixels of four sensors' right edges.

IV. Summary and Discussion

In this article, we presented an MR-compatible CdTe detector module for use in the developed MRC-SPECT-I system. The detector module consists of four CdTe detectors, each with a 1.1 cm $\times$ 2.2 cm $\times$ 2 mm volume and coupled with a custom-designed ASIC with 350 μm $\times$ 350 μm pixels. The detector has less than 5 bad or hot pixels over 8192 pixels. The detector exhibited a spatial resolution capable to sample PRFs from 300-μm pinholes and to observe the impact of 3T MRI over the PRF (Fig. 7).

The 8192 detector pixels have a median energy resolution of 7.0 keV (Fig. 4) and 95% of the pixels have energy resolution better than 9 keV. The performance degrades compared to the ones obtained from the previous non-MRI compatible ERPC detector [36], which recorded an energy resolution of 3.0–6.0 keV. We suspect that the temperature control and higher leakage current may contribute to the degradation of the energy performance. The performance is also not as good as other state-of-the-art detectors as shown in Table II. However, it is worth noting that most of the detectors shown in Table II are not specifically designed for SPECT/MRI applications. Such applications place additional constraints on electronics and cooling. To achieve a compact and MR-compatible design, the detector is using direct air cooling and does not have visible light shielding. Air cooling, instead of actively close loop cooling, presents the challenge for achieving highly efficient temperature control (during the operation, the temperature of sensor can vary from 25 °C to 40 °C). Higher temperature and direct exposure to visible photons will increase leakage current, induces higher electron noise, and ultimately degrades the energy performance. This can be improved with better shielding or incorporating leakage compensation circuitry in the ASIC level.

By using 350-μm pixel size, the detector has a spatial resolution that can sample PRFs from 300-μm pinholes and observe the impact of 3T MRI over the PRF (Fig. 7). For a pixelated semiconductor detector, the spatial resolution is determined by pixel size and charge sharing. It is equal to pixel

TABLE II
SPECIFICATIONS OF CZT/CDTE DETECTORS

Detectors	MRI Compatibility	Pixels	Pixel Size (μm)	ADC Bits	Max Readout Count Rate (cps/mm^2)	Energy Res. (FWHM, keV)	Tech. (μm)
Hexitec [54]	NO	80 ×80	250	14	2.0×10^4	0.8@60	0.35
Timepixe3* [55]	NO	256 ×256	55	10	4.0×10^5	4.07@60	0.13
D2R1-I [56]	NO	16 ×16	300	13	440	0.58@60	0.18
ERPC [36]	NO	32 ×64	350	8	1.6×10^6	3.5@140	0.35
ERPC-MRI	YES	32 ×64	350	8	408	7.0@122	0.35
GMI-CZT [33]	YES	16 ×16	1600	NS	NS	6.0@122	0.80

* Timepixe3 uses 300 μm Si.

size convolved with charge cloud blurring kernel, which has a radius of around 50 μm. This property is well studied [57], [58]. As shown in Fig. 8, PRF is modeled by (3) and the detector resolution in this model is assumed to be the same as the pixel size. It matches the experimental data reasonably well. It indicates the detector resolution is very close to pixel size, as expected.

In this article, instead of evaluating well known CdTe detector spatial properties, we focuses on evaluating how MRI field affects the detector spatial response and how to model this effect accurately, as we show in Figs. 7 and 8. The PRFs become wider and the centroids shift around 0.92 pixel inside a 3T MRI scanner. To model this effect, we have adapted a widely used analytical PRF modeling approach based on (3). The integration volume of (3) is titled at an angle θ (Fig. 3), which is the same as the charge carrier drifting angle. Compared to the previous Monte Carlo approach reported in [32], this method can achieve a reasonable accuracy (Fig. 8) with much less computing cost.

The spatial resolving power is significantly improved compared to other MRI compatible CZT/CdTe detectors, such as GMI-CZT [33], and scintillator detectors [59] shown in Table II. However, the small pixel charge sharing effect [45]–[47] and limited stopping power of 2 mm CdTe degrade the detection efficiency. As we shown in Fig. 6, the detection efficiency of all pixels has a median value of 0.47 and 95% of the pixels have detection efficiency between 0.44 and 0.49, which is significantly less than 1. This impact can be mitigated by using thicker CdTe/CZT (for example, 5 mm CdTe/CZT is typically used) and applying charge sharing correction in ASIC, like Timepixe3 [55] does, or at postprocessing [60], [61].

We also have demonstrated that the detector is capable of operating inside a 3T magnetic field without significant degradation in energy performance (Fig. 5), detection efficiency, or uniformity (Fig. 6) in most of the regions. However, for the pixels at the right edge of each sensor, they were distorted because of the high magnetic field impact over charge transportation. Nevertheless, this effect could be modeled in the similar way as we did for PRF modeling or could be corrected by normalizing raw data using a uniformity map measured inside the MRI scanner. These results were generated using GRE sequence. Based our experience, they should be still valid using other typical MR sequences, such as MPRAGE and Spin echo.

The SPECT system based on this detector module has a bore size of 15.6 cm and is going to be integrated into a clinical 3T system. The performance evaluation of this detector was carried in a 3T MR scanner. To allow the system to be integrated into a high field preclinical scanner, which has a typical bore size of <10 cm, we have to make the detector and system design even more compact, as the one we proposed in MRC-SPECT-II [43]. In addition, all the electrics components of the detector should also be reevaluated, as some components could fail under higher B_0, B_1, and gradient fields inside a preclinical MR scanner. But we believe the correction model derived in this article should still be valid for 7T or higher magnetic field.

The current detector is specifically designed for preclinical SPECT/MRI applications. A few challenges need to be solved for use in clinical imaging applications. First, current ASIC is two-side-buttable and wired-bonded to the PCB board. It only allows to assemble two detector modules in the axial direction, i.e., it can only cover maximum sensing length of around 4.6 cm in the axial direction. To scale system in the transverse direction, we have to tilt the detectors. To develop clinical SPECT system using this detector, we have to redesign the detector packaging using interposer or redesign the ASIC with through-silicon via (TSV) packaging. Second, current maximum readout count rate is 50 cps/pixel which is sufficient for preclinical imaging but it needs significant improvement as the readout rate requirement for human imaging is much higher. Third, the current detector pixel size is 350 μm to achieve sub-500-μm resolution. This greatly increases the circuitry complexity. For a clinical system, we can suggest to increase the pixel size to reduce the number of channels, at the expenses of a reduced spatial resolution, which could still be state of the art. Finally, the price of CdTe/CZT is higher than that of scintillator. Nevertheless, GE has brought Discovery NM530c and NM/CT 870 CZT to the market. Both Siemens and Philips have developed CdTe/CZT-based CT systems. Spectrum Dynamics Medical develops all its systems based on CZT. These commercial successes indicate that, even if the cost of CdTe/CZT detectors is much higher, SPECT systems based on CdTe/CZT technology present a dramatically improved performance and, therefore, are attractive in the medical imaging system market.

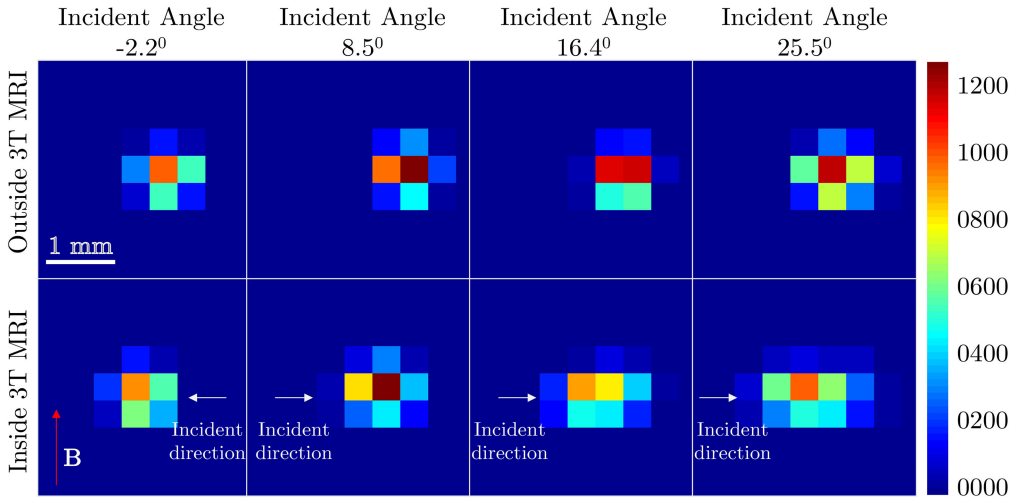

Fig. 7. PRF inside (the first row) and outside (the second row) the 3T MR scanner. In comparison to the PRFs outside MRI, weighted center of the PRFs inside MRI shifts around 0.92 pixel, i.e., 0.33 mm to the left.

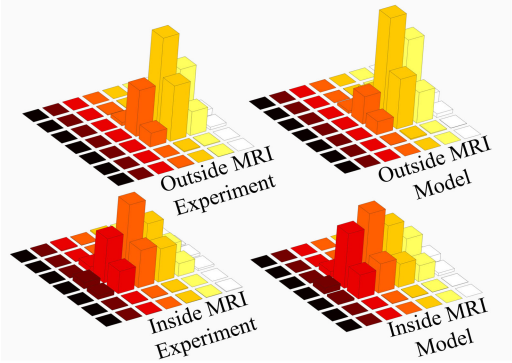

Fig. 8. Comparison of the measured PRF and modeled PRF (both are normalized); the root of mean-square error ([defined in (7)]) of modeled PRFs is around 5% compared to the measured ones, and the weighted center difference is less than 0.10 pixel, i.e., 0.035 mm.

V. Conclusion

In this article, we presented a highly pixelated CZT detector dedicated for SPECT/MRI imaging applications. The detector has a 350-μm pixel size and achieves a median energy resolution of 7.0 keV over 8192 pixels. The detector performance does not significantly degrade when it is operated inside a 3T MRI scanner. We also proposed analytical model that can accurately model the spatial response inside a 3T MRI clinical scanner.

References

[1] M. S. Judenhofer *et al.*, "Simultaneous PET-MRI: A new approach for functional and morphological imaging," *Nat. Med.*, vol. 14, no. 4, pp. 459–465, 2008.

[2] H. F. Wehrl, M. S. Judenhofer, A. Thielscher, P. Martirosian, F. Schick, and B. J. Pichler, "Assessment of MR compatibility of a PET insert developed for simultaneous multiparametric PET/MR imaging on an animal system operating at 7 T," *Magn. Reson. Med.*, vol. 65, no. 1, pp. 269–279, 2011.

[3] G. Delso *et al.*, "Performance measurements of the Siemens mMR integrated whole-body PET/MR scanner," *J. Nucl. Med.*, vol. 52, no. 12, pp. 1914–1922, 2011.

[4] A. M. Grant, T. W. Deller, M. M. Khalighi, S. H. Maramraju, G. Delso, and C. S. Levin, "NEMA NU 2-2012 performance studies for the SiPM-based ToF-PET component of the GE SIGNA PET/MR system," *Med. Phys.*, vol. 43, no. 5, pp. 2334–2343, 2016.

[5] G. Delso, M. Khalighi, M. Hofbauer, M. Porto, P. Veit-Haibach, and G. von Schulthess, "Preliminary evaluation of image quality in a new clinical ToF-PET/MR scanner," *EJNMMI Phys.*, vol. 1, no. 1, p. A41, 2014.

[6] S. Houshmand, T. Werner, and A. Alavi, "Advances in the PET/CT and PET/MRI hybrid imaging: An update on instrumentation and techniques of quantitation," *J. Nucl. Med.*, vol. 57, no. s2, p. 1288, 2016.

[7] M. Wilks, X. Zhang, J. Ouyang, G. El Fakhri, N. Alpert, and Q. Li, "True blood flow imaging in tumors using spatially constrained PET/MRI modeling," *J. Nucl. Med.*, vol. 57, no. s2, p. 436, 2016.

[8] M. Sollini *et al.*, "PET/MRI in infection and inflammation," *Seminars Nucl. Med.*, vol. 48, no. 3, pp. 225–241, 2018.

[9] T. A. Hope *et al.*, "State of the art PET/MRI: Applications and limitations—Summary of the first ISMRM/SNMMI co-provided workshop on PET/MRI," *J. Nucl. Med.*, vol. 62, no. 2, pp. 1340–1346, 2019.

[10] N. S. Kwatra, R. Lim, M. S. Gee, L. J. States, A. Vossough, and E. Y. Lee, "PET/MR Imaging: Current updates on pediatric applications," *Magn. Reson. Imag. Clin.*, vol. 27, no. 2, pp. 387–407, 2019.

[11] K. M. Ropella-Panagis, N. Seiberlich, and V. Gulani, "Magnetic resonance fingerprinting: Implications and opportunities for PET/MR," *IEEE Trans. Radiat. Plasma Med. Sci.*, vol. 3, no. 4, pp. 388–399, Jul. 2019.

[12] F. C. Michelotti *et al.*, "PET/MRI enables simultaneous in vivo quantification of β-cell mass and function," *Theranostics*, vol. 10, no. 1, pp. 398–410, 2020.

[13] C. E. Mader, T. Fuchs, D. A. Ferraro, and I. A. Burger, "Potential clinical applications of PET/MR," *IEEE Trans. Radiat. Plasma Med. Sci.*, vol. 4, no. 3, pp. 293–299, May 2020.

[14] B. Hutton *et al.*, "INSERT: A novel clinical scanner for simultaneous SPECT/MRI brain studies," in *Proc. IEEE Nucl. Sci. Symp. Med. Imag. Conf. (NSS/MIC)*, Atlanta, GA, USA, 2017, pp. 1–2.

[15] A. T. Tao, M. D. Noseworthy, and T. H. Farncombe, "Measuring the effect of CZT detector materials on MRI field homogeneity," in *Proc. IEEE Nucl. Sci. Symp. Med. Imag. Conf. (NSS/MIC)*, Seattle, WA, USA, 2014, pp. 1–5.

[16] A. M. Samoudi *et al.*, "Analysis of eddy currents induced by transverse and longitudinal gradient coils in different tungsten collimators geometries for SPECT/MRI integration," *Magn. Reson. Med.*, vol. 74, no. 6, pp. 1780–1789, 2015.

[17] A. M. Samoudi *et al.*, "Simulated design strategies for SPECT collimators to reduce the eddy currents induced by MRI gradient fields," *IEEE Trans. Nucl. Sci.*, vol. 62, no. 5, pp. 2017–2022, Oct. 2015.

[18] S. R. Cherry, "Multimodality imaging: Beyond PET/CT and SPECT/CT," *Seminars Nucl. Med.*, vol. 39, no. 5, pp. 348–353, 2009.

[19] K. Deprez, S. Vandenberghe, K. Van Audenhaege, J. Van Vaerenbergh, and R. Van Holen, "Rapid additive manufacturing of MR compatible multipinhole collimators with selective laser melting of tungsten powder," *Med. Phys.*, vol. 40, no. 1, 2013, Art. no. 012501.

[20] K. Van Audenhaege, R. Van Holen, C. Vanhove, and S. Vandenberghe, "Collimator Design for a Multipinhole Brain SPECT Insert for MRI," *Med. Phys.*, vol. 42, no. 11, 2015, Art. no. 667989.

[21] M. Carminati *et al.*, "SPECT/MRI INSERT compatibility: Assessment, solutions, and design guidelines," *IEEE Trans. Radiat. Plasma Med. Sci.*, vol. 2, no. 4, pp. 369–379, Jul. 2018.

[22] S. Yamamoto *et al.*, "Development of a high-resolution Si-PM-based gamma camera system," *Phys. Med. Biol.*, vol. 56, no. 23, p. 7555, 2011.

[23] S. Yamamoto, T. Watabe, Y. Kanai, H. Watabe, and J. Hatazawa, "Development of an optical fiber-based MR compatible gamma camera for SPECT/MRI systems," *IEEE Trans. Nucl. Sci.*, vol. 62, no. 1, pp. 76–81, Feb. 2015.

[24] D. Philippov, A. Ilyin, V. Belyaev, E. Popova, P. Buzhan, and A. Stifutkin, "SiPM-MAROC gamma-camera prototype with monolithic NaI(Tl) scintillator," *EJNMMI Phys.*, vol. 2, no. S1, p. A49, 2015.

[25] M. Occhipinti *et al.*, "Characterization of the detection module of the INSERT SPECT/MRI clinical system," *IEEE Trans. Radiat. Plasma Med. Sci.*, vol. 2, no. 6, pp. 554–563, Nov. 2018.

[26] M. Carminati *et al.*, "Experimental validation of a preclinical SPECT/MR insert," in *Proc. IEEE Nucl. Sci. Symp. Med. Imag. Conf. (NSS/MIC)*, Atlanta, GA, USA, 2017, pp. 1–3.

[27] D. Salvado *et al.*, "Development of a practical calibration procedure for a clinical SPECT/MRI system using a single INSERT prototype detector and multimini slit-slat collimator," *IEEE Trans. Radiat. Plasma Med. Sci.*, vol. 2, no. 4, pp. 380–386, Jul. 2018.

[28] M. Carminati *et al.*, "Validation and performance assessment of a preclinical SiPM-based SPECT/MRI insert," *IEEE Trans. Radiat. Plasma Med. Sci.*, vol. 3, no. 4, pp. 483–490, Jul. 2019.

[29] M. Carminati *et al.*, "Clinical SiPM-based MRI-compatible SPECT: Preliminary characterization," *IEEE Trans. Radiat. Plasma Med. Sci.*, vol. 4, no. 3, pp. 371–377, May 2020.

[30] B. F. Hutton *et al.*, "Development of clinical simultaneous SPECT/MRI," *Brit. J. Radiol.*, vol. 91, no. 1081, 2018, Art. no. 20160690.

[31] M. J. Hamamura *et al.*, "Development of an MR-compatible SPECT system (MRSPECT) for simultaneous data acquisition," *Phys. Med. Biol.*, vol. 55, no. 6, pp. 1563–1575, 2010.

[32] J. W. Tan, L. Cai, and L. J. Meng, "Experimental study of the response of CZT and CdTe detectors of various thicknesses in strong magnetic field," *Nucl. Instrum. Methods Phys. Res. A, Accelerators Spectrometers Detectors Assoc. Equip.*, vol. 652, no. 1, pp. 153–157, 2011.

[33] D. J. Wagenaar *et al.*, "Development of MRI-compatible nuclear medicine imaging detectors," in *Proc. IEEE Nucl. Sci. Symp. Conf. Rec.*, vol. 3. San Diego, CA, USA, 2006, pp. 1825–1828.

[34] D. Meier, D. Wagenaar, S. Chen, J. Xu, J. Yu, and B. M. W. Tsui, "A SPECT camera for combined MRI and SPECT for small animals," *Nucl. Instrum. Methods Phys. Res. A, Accelerators Spectrometers Detectors Assoc. Equip.*, vol. 652, no. 1, pp. 731–734, 2011.

[35] B. Tsui, J. Xu, A. Rittenbach, J. W. Hugg, and K. B. Parnham, "Development of a second-generation whole-body small-animal spect/mr imaging system," in *Hybrid Imaging in Cardiovascular Medicine*. Boca Raton, FL, USA: CRC Press, 2017, pp. 57–74.

[36] L.-J. Meng, J. Tan, K. Spartiotis, and T. Schulman, "Preliminary evaluation of a novel energy-resolved photon-counting gamma ray detector," in *Proc. IEEE Nucl. Sci. Symp. Conf. Rec.*, 2008, pp. 308–314.

[37] "ACRORAD," 2020. [Online]. Available: https://www.acrorad.co.jp/index_en/company_en.html

[38] G. F. Knoll, *Appendix D, Radiation Detection and Measurement*. Hoboken, NJ, USA: Wiley, 2010.

[39] M. Silosky, V. Johnson, C. Beasley, and S. C. Kappadath, "Characterization of the count rate performance of modern gamma cameras," *Med. Phys.*, vol. 40, no. 3, 2013, Art. no. 032502.

[40] Z.-P. Liang and P. C. Lauterbur, *Principles of Magnetic Resonance Imaging: A Signal Processing Perspective*. Bellingham, WA, USA: SPIE Opt. Eng. Press, 2000.

[41] N. U. Schramm, G. Ebel, U. Engeland, T. Schurrat, M. Behe, and T. M. Behr, "High-resolution spect using multipinhole collimation," *IEEE Trans. Nucl. Sci.*, vol. 50, no. 3, pp. 315–320, Jun. 2003.

[42] E. C. Frey and B. M. W. Tsui, "Collimator-detector response compensation in SPECT," in *Quantitative Analysis in Nuclear Medicine Imaging*. Boston, MA, USA: Springer, 2006, pp. 141–166.

[43] X. Lai and L.-J. Meng, "Simulation study of the second-generation MR-compatible SPECT system based on the inverted compound-eye gamma camera design," *Phys. Med. Biol.*, vol. 63, no. 4, 2018, Art. no. 045008.

[44] A. Castoldi, E. Gatti, V. Manzari, and P. Rehak, "Performance of silicon drift detectors in a magnetic field," *Nucl. Instrum. Methods Phys. Rec. A, Accelerators Spectrometers Detectors Assoc. Equip.*, vol. 399, nos. 2–3, pp. 227–243, 1997.

[45] A. Burger *et al.*, "Defects in CZT crystals and their relationship to gamma-ray detector performance," *Nucl. Instrum. Methods Phys. Res. A, Accelerators Spectrometers Detectors Assoc. Equip.*, vol. 448, no. 3, pp. 586–590, 2000.

[46] A. E. Bolotnikov *et al.*, "Te inclusions in CZT detectors: New method for correcting their adverse effects," *IEEE Trans. Nucl. Sci.*, vol. 57, no. 2, pp. 910–919, Apr. 2010.

[47] A. E. Bolotnikov *et al.*, "Characterization and evaluation of extended defects in CZT crystals for gamma-ray detectors," *J. Cryst. Growth*, vol. 379, pp. 46–56, Sep. 2013.

[48] Y. F. Du, Z. He, W. Li, G. F. Knoll, and D. K. Wehe, "Monte carlo investigation of the charge sharing effects in 3-D position sensitive cdznte gamma ray spectrometers," *IEEE Trans. Nucl. Sci.*, vol. 46, no. 4, pp. 844–847, Aug. 1999.

[49] C. M. H. Chen, S. E. Boggs, A. E. Bolotnikov, W. R. Cook, F. A. Harrison, and S. M. Schindler, "Numerical modeling of charge sharing in CdZnTe pixel detectors," *IEEE Trans. Nucl. Sci.*, vol. 49, no. 1, pp. 270–276, Feb. 2002.

[50] M. Chmeissani *et al.*, "Charge sharing measurements of pixilated CdTe using medipix-II chip," in *Proc. 21st IEEE Instrum. Meas. Technol. Conf.*, vol. 1. Como, Italy, 2004, pp. 787–791.

[51] A. Meuris, O. Limousin, and C. Blondel, "Charge sharing in CdTe pixilated detectors," *Nucl. Instrum. Methods Phys. Res. A, Accelerators Spectrometers Detectors Assoc. Equip.*, vol. 610, no. 1, pp. 294–297, 2009.

[52] M. C. Veale *et al.*, "An ASIC for the study of charge sharing effects in small pixel CdZnTe X-ray detectors," *IEEE Trans. Nucl. Sci.*, vol. 58, no. 5, pp. 2357–2362, Oct. 2011.

[53] J. C. Kim *et al.*, "Charge sharing in common-grid pixelated cdznte detectors," *Nucl. Instrum. Methods Phys. Res. A, Accelerators Spectrometers Detectors Assoc. Equip.*, vol. 654, no. 1, pp. 233–243, 2011.

[54] L. Jones, P. Seller, M. Wilson, and A. Hardie, "HEXITEC ASIC—A pixellated readout chip for CZT detectors," *Nucl. Instrum. Methods Phys. Res. A, Accelerators Spectrometers Detectors Assoc. Equip.*, vol. 604, nos. 1–2, pp. 34–37, 2009.

[55] T. Poikela *et al.*, "Timepix3: A 65K channel hybrid pixel readout chip with simultaneous ToA/ToT and sparse readout," *J. Instrum.*, vol. 9, no. 05, 2014, Art. no. C05013.

[56] D. Baudin *et al.*, "D^2R_1: A 2-dimensional X-ray detector for CdTe based fine pitch and high energy resolution imaging spectroscopy," *IEEE Trans. Nucl. Sci.*, vol. 65, no. 7, pp. 1408–1415, Jul. 2018.

[57] M. Ruat and C. Ponchut, "Characterization of a pixelated CdTe X-ray detector using the timepix photon-counting readout chip," *IEEE Trans. Nucl. Sci.*, vol. 59, no. 5, pp. 2392–2401, Oct. 2012.

[58] X. Zheng, Z. Cheng, M. J. Deen, and H. Peng, "Improving the spatial resolution in czt detectors using charge sharing effect and transient signal analysis: Simulation study," *Nucl. Instrum. Methods Phys. Res. A, Accelerators Spectrometers Detectors Assoc. Equip.*, vol. 808, pp. 60–70, Feb. 2016.

[59] C. Bouckaert, S. Vandenberghe, and R. Van Holen, "Evaluation of a compact, high-resolution SPECT detector based on digital silicon photomultipliers," *Phys. Med. Biol.*, vol. 59, no. 23, pp. 7521–7539, 2014.

[60] L. Abbene *et al.*, "Dual-polarity pulse processing and analysis for charge-loss correction in cadmium–zinc–telluride pixel detectors," *J. Synchrotron Radiat.*, vol. 25, no. 4, pp. 1078–1092, 2018.

[61] S. L. Bugby, K. A. Koch-Mehrin, M. C. Veale, M. D. Wilson, and J. E. Lees, "Energy-loss correction in charge sharing events for improved performance of pixellated compound semiconductors," *Nucl. Instrum. Methods Phys. Res. A, Accelerators Spectrometers Detectors Assoc. Equip.*, vol. 940, pp. 142–151, Oct. 2019.